

Hierarchical Mesoporous Hematite with “Electron-Transport Channels” and Its Improved Performances in Photocatalysis and Lithium Ion Batteries

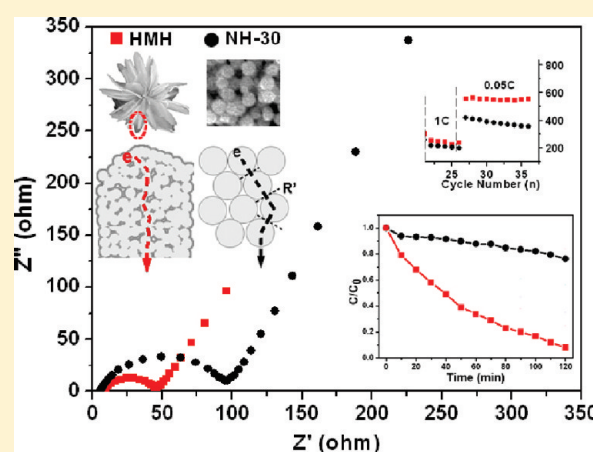
Wei Zhou,[†] Lijuan Lin,[†] Weijie Wang,[‡] Linlin Zhang,[†] Qiong Wu,[†] Jinghong Li,^{*,‡} and Lin Guo^{*,†}

[†]School of Chemistry and Environment, Beihang University, Beijing 100191, China

[‡]Department of Chemistry, Key Laboratory of Bioorganic Phosphorus Chemistry & Chemical Biology, Tsinghua University, Beijing 100084, China

 Supporting Information

ABSTRACT: Hierarchical mesoporous hematite ($\alpha\text{-Fe}_2\text{O}_3$) assembled by porous nanoplates has been synthesized by heating the iron oxyhydroxide (FeOOH) precursor. The plates of the hematite, 100–300 nm in width, 500 nm in length, were composed of single crystal long particles with an average diameter of 15 nm. High-resolution transmission electron microscopy results show that these particles have grown or linked together, forming netlike substructures (like “electron-transport channels”). The fabricated hematite has a high specific surface area $\sim 116\text{ m}^2/\text{g}$ with an average pore size of 7.85 nm. The photocatalytic and electrochemical properties of the sample were investigated, showing improved performances because of the high specific surface area, rich mesopores, and electron-transport channels of the as-prepared spatial structure. The designed hierarchical mesoporous structure shows potential applications in photocatalysis and lithium ion batteries.



Research on semiconductor nanomaterials has aroused great interests because of their ideal environmental remediation by photocatalytic degradation of pollutants under light irradiation.^{1,2} Among various semiconductors, some oxides such as zinc oxide, titanium dioxide, and iron oxide were largely studied with the advantages of low cost and environmentally benign properties.^{3–5} The most important thing related to photocatalysis focuses on improving the degradation rate efficiently. Two major ways have been verified by many researchers. One effective way is to reduce the recombination of photo-generated electron–hole pairs by adjusting the component of the semiconductor.^{6–8} As the recombination remains a big problem in the photocatalytic process, usually researchers disperse fine particles of transition metals or their oxides on the surfaces of the conductor in order to reduce the recombination of electrons and holes by accelerating the electron transfer through surface particles.^{6–8}

Fabricating suitable structures with high specific surface area (SSA) is another smart method because the semiconductor nanomaterials with large surface will absorb more pollutants, provide more reaction active sites, even reduce the recombination of electrons and holes, and thus improve the degradation rate. Take hematite ($\alpha\text{-Fe}_2\text{O}_3$) nanomaterials, for example. Although a variety of structures have been synthesized including 3D nanopropeller, single-crystal nanorings, symmetrical dendritic structures, single

crystal nanorods and many other structures, only two types of structures can afford high SSA: the hierarchical structure and the porous or hollow structure.^{9–15} Especially, some researchers found that mesoporous hematite materials with well improved photocatalytic properties had much higher SSAs.^{14,15} Therefore, it is necessary to combine these two structures together, that is, to synthesize hierarchical mesoporous structures for advanced photocatalytic materials. Additionally, the solid-state thermal annealing method could create porous structures with high SSAs, which might improve the related photocatalytic and other performances.^{16,17}

Herein, we deliberately designed a novel flowerlike structure of hematite composed of one-dimensional (1D) mesoporous nanoplates by a solid-state thermal annealing method. On one hand, it was a hierarchical mesoporous structure with an average pore size of 7.85 nm and SSA $\sim 116\text{ m}^2/\text{g}$, higher than most reported hierarchical or hollow structures. On the other hand, the obtained netlike substructures of the nanoplates could serve as “electron transfer channels”, which would reduce the recombination of electrons and holes. Instead of the first method that increased the photocatalytic efficiency by adjusting the

Received: February 3, 2011

Revised: March 4, 2011

Published: March 23, 2011

component, we fabricated fine structures to reduce the recombination by increasing electron transfer. Instead of special methods, such as hydrothermal or solvothermal methods for hierarchical structures and expensive block-copolymer-templated method for mesoporous structures,^{14,15,18,19} we simply use a mild chemical method to fabricate hierarchical α -FeOOH precursor with cetyltrimethyl amine bromide (CTAB) as soft templates. By choosing heating time for the precursor, an optimal hierarchical mesoporous hematite (HMH) was obtained with high SSA, rich mesopores, and “electron-transport channels”.

To verify the advantage of the obtained structure, the photocatalytic controlled experiments were taken on degradation of rhodamine B (RB) using the as-prepared sample and the purchased uniform nanoparticles (NPs), ~ 30 nm in diameter. As a common material in our daily life, hematite materials have been widely used in fields of lithium ion batteries, sensors, optical switching, targeted cancer therapy, and multimodal imaging besides photocatalysis.^{20–23} Therefore, another demonstration on the structure advantage was carried out. Some controlled experiments on lithium ion batteries were taken using the HMH sample or the purchased NPs as electrode materials. Those experiment results show promising applications of the as-prepared hierarchical mesoporous hematite with electron transfer channels in catalytic and lithium ion battery fields.

■ EXPERIMENTAL METHODS

Synthesis of α -FeOOH Precursor and HMH Sample. In a typical experiment, all reagents were used without further purification. Ferrum chloride tetrahydrate (0.5 mmol) and 1.0 g of CTAB were dissolved in 40 mL of EG at room temperature. Ethanol solution (20 mL) with 0.5 mmol of sodium hydroxide was then added. The mixture was further aged for 1 h under magnetic stirring. An orange-colored solution thus obtained was heated constantly with boiling bubbles and kept for 5 h. The sample cooling down naturally was washed with ethanol and deionized water. By centrifugation, the powder was dried at 60 °C overnight, and an orange-yellow α -FeOOH precursor was collected. The dry precursor was calcined at 350 °C for 3 h in air, and then a reddish brown hematite powder was obtained (labeled as HMH sample).

Characterization. X-ray powder diffraction (XRD) patterns of the samples were recorded on a Rigaku Dmax2200 diffractometer with Cu K α radiation ($\lambda = 1.5416$ Å). The morphology of the samples was studied by a field-emission gun (FEG) scanning electron microscope (Hitachi S-4800, 10 kV) with the specimen obtained by dropping thick suspension on the silicon slices. Transmission electron microscopy (TEM) and high-resolution TEM (HRTEM) investigations were carried out by a JEOL JEM-2100F microscope. The Brunauer–Emmett–Teller (BET) specific surface area and pore size distribution were performed by N₂ gas adsorption using a Quanta Chrome (Nova 2200e) surface area and pore size analytical instrument.

Photocatalysis Measurement. The as-prepared FeOOH precursor and hematite samples as well as the purchased nanoparticle hematite with an average diameter of 30 nm (Aladdin Inc., labeled as NH-30) were used to investigate the degradation of RB, respectively. The sample (30 mg) was added to 60 mL of RB aqueous solution (1.0×10^{-5} M) and then magnetically stirred in the dark for 2 h, making full adsorption and uniform dispersion. The solution was then exposed to UV light irradiation with a distance of 20 cm from a 250-W

high-pressure mercury lamp at room temperature. Every 10 min, 4 mL of solution was withdrawn from the test tube for analysis. The absorption spectra of the solutions were measured by a Lambda 950 (Perkin-Elmer Instruments) ultraviolet–visible spectrophotometer. Some controlled experiments were performed with different catalysts and without any catalyst. The used as-prepared hematite samples included an HMH sample and other hematite samples by calcinating FeOOH precursor for 1 h and 5 h (labeled as HMH-1 h and HMH-5 h, respectively).

Electrochemical Characterization. Electrochemical experiments were performed in CR2023-type coin cells, using lithium as the counter electrode. The working electrode was prepared by mixing the HMH series samples or the NH-30 sample, acetylene black, and the binder (polytetrafluoroethylene) at a weight ratio of 70:15:15 on pure Cu foil. The electrolyte consisted of a solution of 1 M LiPF₆ in a mixture of ethylene carbonate (EC)/dimethyl carbonate (DMC)/diethyl carbonate (DEC) (1:1:1 by volume). The cells were dried at 90 °C for 12 h and then assembled in an argon-filled glovebox. The galvanostatic charge/discharge experiment was performed between 0.01 and 3.0 V at a constant current density of 50 mA/g on a Roofer Battery Tester (Shenzhen, China). The electrochemical impedance measurements were carried out on a Parstat 2273 Potentionstat/Galvanostat (Advanced Measurement Technology Inc., USA). The Nyquist plots were recorded potentiostatically by applying an AC voltage of 5 mV amplitude in the 100 kHz to 100 mHz frequency range. The cyclic voltammograms (CVs) were recorded from 3.0 to 0 V at a scan rate of 0.1 mV/s, using an electrochemical workstation (CHI 802B, CH Instruments, US). All above electrochemical measurements were taken at room temperature.

■ RESULTS AND DISCUSSION

Characterization of the FeOOH and the HMH Samples.

Figure 1 shows the XRD patterns of the precursor and the as-prepared sample.

In Figure 1a, all diffraction peaks were labeled and could be indexed to the orthorhombic phase of α -FeOOH (JCPDS 81-0464). In comparison with the standard pattern, the intensity of the (021) peak was increased, indicating most crystals grew along the direction of [021] axis. By annealed at 350 °C for 3 h, the rhombohedral hematite (α -Fe₂O₃) sample was obtained with the XRD pattern in Figure 1b agreeing well with the standard card (JCPDS 33-0664). It has been widely reported that the α -Fe₂O₃ phase originates from α -FeOOH (goethite) dehydration in calcinations process.^{24,25}

The morphologies of the FeOOH precursor and the HMH sample were shown in Figure 2. Figure 2a shows an overview of the microflower particles about 2–5 μ m in diameter. The magnified image in Figure 2b shows that the flowers are composed of 1D plates with the width of 300–500 nm and the length up to several micrometers. The inset in Figure 2b exhibits rough surface of one nanoplate. After calcinations, the HMH sample maintained the same microflower morphology only with shortened plates, about 100–300 nm in width, 500 nm in length, as shown in Figure 2c. The magnified image in Figure 2d shows that the nanoplates are composed of NPS (~ 15 nm in diameter), which will further be revealed by HRTEM image.

To further reveal the morphologies of FeOOH precursor and HMH samples, TEM and HRTEM characterizations were taken. Figure S1a of Supporting Information shows several overlapped plates from a FeOOH microflower with some angles at the tip in

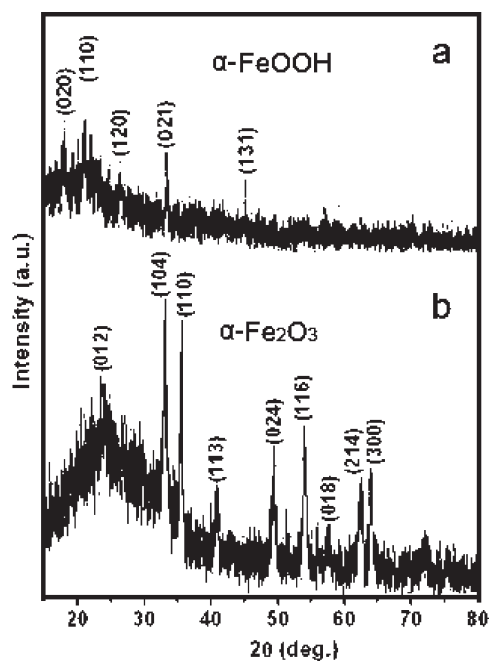


Figure 1. XRD patterns of the α -FeOOH precursor (a) and the HMH sample (b).

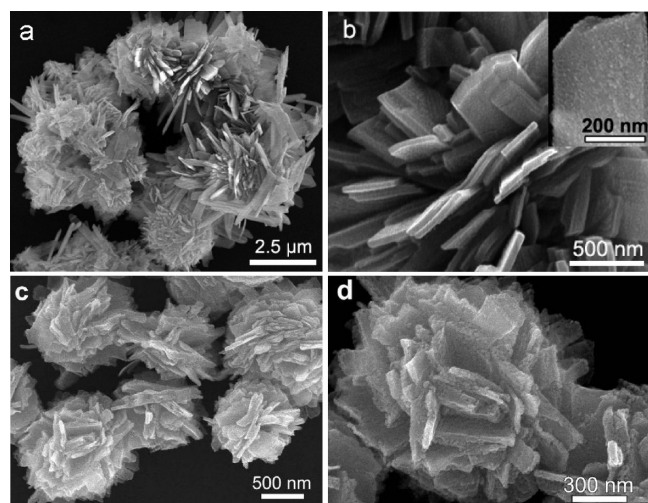


Figure 2. (a) SEM image of the FeOOH precursor. (b) Magnified SEM image of a FeOOH flower; the inset shows a typical nanoplate with rough surface. (c) SEM image of HMH sample with shortened plates. (d) Magnified SEM image for a typical HMH flower composed of many tiny particles.

accordance with the SEM image in Figure 2b. Figure S1b of Supporting Information shows the magnified image of part of the plate, exhibiting the polycrystalline plate was formed by many particles. Parts c and d of Figure S1 of Supporting Information show the HRTEM images corresponding to the different parts of the plate. It could be found that the plate was not well crystallized with partial unclear crystal lattices. The measured spacing of 0.25 nm can be indexed to the planes of (021)_{FeOOH} in accordance with the increased peak of (021) in Figure 1a. These particles about 5 nm in diameter might have grown together, causing mesopores, which would be revealed later.

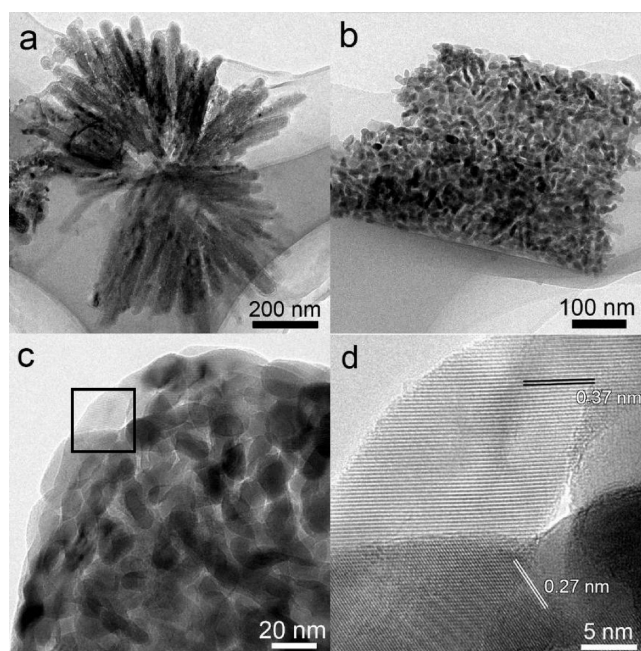


Figure 3. TEM and HRTEM images of the HMH sample. (a) A typical flowerlike particle. (b) Two broken plates composed of nanoparticles. (c) Magnified tip of one plate, showing netlike structure. (d) HRTEM image corresponding to the frame region in Figure 3c.

Figure 3a shows a typical TEM image for a HMH flower. It could be found that the hematite structure remains the same as the precursor. Figure 3b shows that two broken nanoplates are composed of long NPs with size of $\sim 10 \times 20$ nm \times nm, forming netlike structure. Figure 3c shows magnified tips of one plate. Both parts b and c of Figure 3 show clearly the voids about several nanometers. Figure 3d corresponds to the framed region in Figure 3c. The spacing of 0.37 and 0.27 nm can be indexed to the planes of (012)_{Fe₂O₃} and (104)_{Fe₂O₃}, respectively. As displayed in parts c and d of Figure 3, the structure of note is that these long particles either grow together or connect tightly to form netlike substructures, like “electron-transport channels”. The advantage of the substructure will be demonstrated.

Characterizations on the FeOOH precursor and HMH samples above reveal an ideal mesoporous structure. It is further verified by the N₂ adsorption–desorption isotherms and the pore size distributions in Figure 4. Meanwhile, in order to investigate the advantage of the hierarchical mesoporous structure, a purchased nanoparticle hematite with an average diameter of 30 nm (labeled as NH-30) was used to compare with the as-prepared samples. The SEM image and XRD pattern for the purchased NPs were shown in Figure S2 of Supporting Information.

The three curves in Figure 4a can be considered as type IV isotherms. The isotherms for the HMH and NH-30 nm samples were similar to the curves reported before for hematite samples.^{5,18,19} The surface areas estimated from the BET method are 225, 116, and 47 m²/g for FeOOH precursor, HMH, and NH-30 samples, respectively. It is obvious that the designed hierarchical mesoporous samples have higher SSA (225 and 116 m²/g) than NH-30 sample (~ 30 nm in diameter, 47 m²/g). They are also higher than those for reported flowerlike hematite samples, ~ 10 –70 m²/g,^{5,18–20,26,27} and hollow NPs, ~ 40 m²/g.²⁸ Obviously, we successfully synthesized an excellent structure with high SSA.

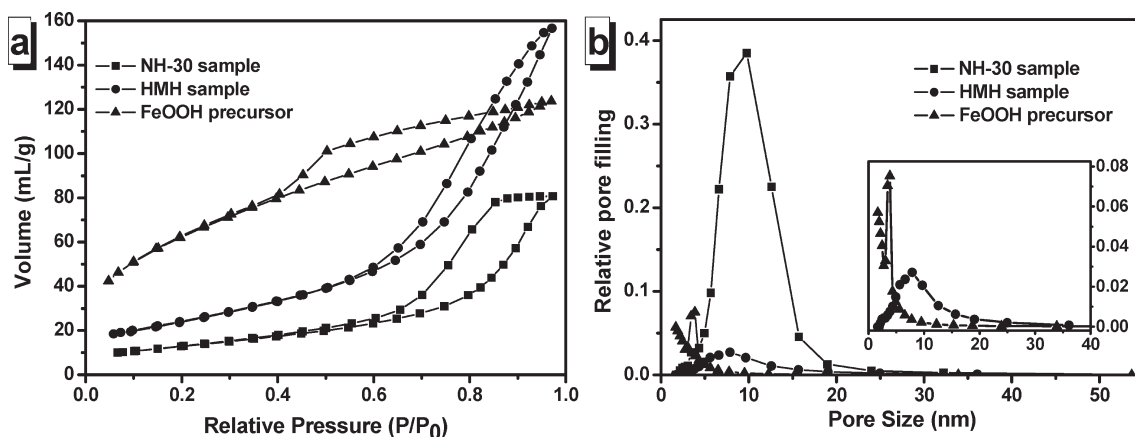


Figure 4. Nitrogen adsorption–desorption isotherms (a) and pore size distributions (b) for the FeOOH precursor, HMH sample, and the purchased nanoparticle hematite (labeled as NH-30). The inset shows the magnified part of part b.

As shown in Figure 4b and its inset, the pore size analysis on desorption data based on the Barrett–Joyner–Halenda (BJH) method, demonstrated clearly that the pores of the hematite increased from 3.85 nm (FeOOH precursor) to 7.85 nm (HMH sample), while the NH-30 sample had an average pore size of 7.90 nm. It is certain that the heat treatment brought increasing pores for the oxides from the hydroxides, and the similar phenomenon has been reported before.^{29,30} As for the increasing pore size, it is also reasonable that the hematite sample has a decreasing SSA (116 m²/g) compared with the FeOOH precursor (225 m²/g).

Growth Mechanism. On the basis of the above structure characterizations, probable growth mechanisms for the FeOOH precursor and HMH sample were proposed, as shown in Figure 5.

First, there was a little water in the mixed solvents of ethanol and EG, accompanying with a trace of hydroxyls, easily forming FeOOH NPs seeds. The reaction can be described as follows



To keep stable, the prior forming FeOOH seeds would aggregate and grow together in a very short time, forming FeOOH NPs ~5 nm in diameter as revealed by parts c and d of Figure S1 of Supporting Information (Figure 5a). Meanwhile, the CTAB molecular size (~1.2 nm) is comparable to the size of FeOOH NPs,³¹ serving as the surface modified agents (Figure 5a). As reported, CTAB is an ideal surface modification for fabrication of 1D nanostructures.^{32,33} When we reduced the quantity of CTAB in the reaction system, the length of 1D nanoplates was obviously reduced (as shown in Figure S3 of Supporting Information). Under the direction of CTAB molecules, these particles would further aggregate to fabricate nanoplates with angular tips (Figure 5b). The angular tip as circled in Figure 5b might be the original particle offering growth site for nanoplates with the modification of CTAB molecules. Obviously, it is hard for those particles to connect or grow tightly as the isolation of CTAB molecules, just as depicted in parts c and d of Figure S1 of Supporting Information. As heated for 5 h at the boiling point of the mixed solvent of ethanol and EG, these nanoplates aggregated to form flowerlike structures, keeping a low-energy and stable condition (Figure 5c). When the FeOOH precursor was calcinated, the HMH sample still remained the similar flowerlike

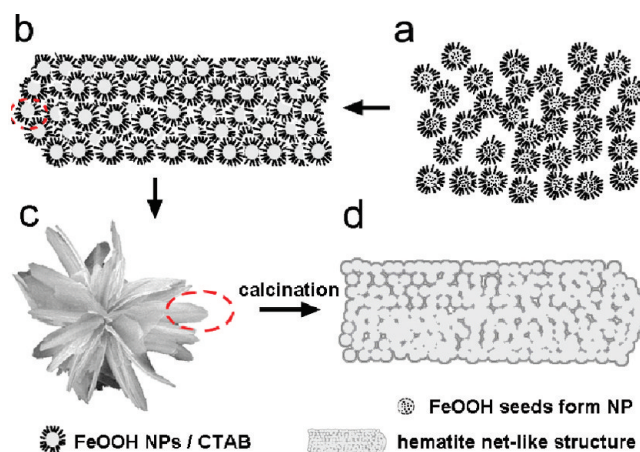


Figure 5. Formation mechanism for the HMH sample. (a) FeOOH seeds aggregated and grew to particles, capped by CTAB molecules. (b) The particles were directed by CTAB molecules, growing into 1D FeOOH nanoplates. (c) Flowerlike FeOOH precursor was formed by accumulated nanoplates. (d) The HMH sample remains the same flowerlike structure as the precursor. Some NPs in the plates grew together, forming netlike substructures under heat treatment. Part d was the enlarged part of the red circle in part c.

structure. However, some particles in the nanoplates (part of the flowers) grew together forming netlike substructures, and mesopores among these particles became bigger under heat treatment (Figure 5d), as demonstrated by the HRTEM and BET results above.

Photocatalytic and Electrochemical Properties. The as-prepared HMH and the purchased NH-30 samples were used as electrode materials to measure their electrochemical impedances. The electron transport could benefit more from the structure of the HMH sample than from NH-30 sample. It was verified by the result of the Nyquist plots in Figure 6.

Figure 6 shows AC impedance spectra of the HMH and NH-30 samples. They have similar plots with one semicircle in the high frequency region and an incline straight line in the low frequency. Both of them can be analyzed with the same equivalent circuit mode (the inset left above of Figure 6). R_s , R_{ct} , Z_{w} , and CPE represent resistance of the electrolytes, charge-transfer resistance, Warburg resistance, and constant phase element,

respectively.³⁴ The semicircle in the middle frequency region is attributable to the charge-transfer resistance (R_{ct}), showing the charge transfer through the electrode/electrolyte interface. The intercept at Z' in high frequency regions is related to the resistance of the electrolytes (R_s). From the plots, it is obvious that the radius of the semicircle of the HMH sample is much smaller than that of the NH-30 sample. It can be deduced that the HMH sample improves the conductivity of the electrode. That is, the designed hierarchical mesoporous structure contributes to the improvement in the electron transport. The explanation was illustrated in the right inset of Figure 6. The netlike substructures of the plates in the HMH sample will improve the electron transport, such as electron-transport channels. As for the NH-30 sample, the electrons transferred difficultly, because of the contact resistance among these particles. Therefore, the mesoporous hierarchical structure leads to the low resistance of the related electrode.

By taking advantage of the high SSA, the mesopores, and the electron-transport channels of the HMH sample, photocatalytic performances were investigated with the degradation of RB using high-pressure mercury lamp at room temperature. The degradation rate was verified using the HMH sample as catalyst by the

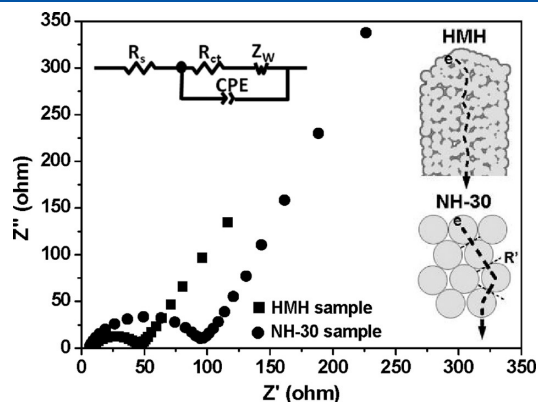


Figure 6. Nyquist plots of the HMH (squares) and the NH-30 sample (circles) by applying an AC voltage of 5 mV in the 100 mHz to 100 kHz frequency range. The inset left above is shown an equivalent circuit mode plot, while the right one illustrates the electron-transport path in the HMH and NH-30 samples (R' represents contact resistance between two particles of NH-30).

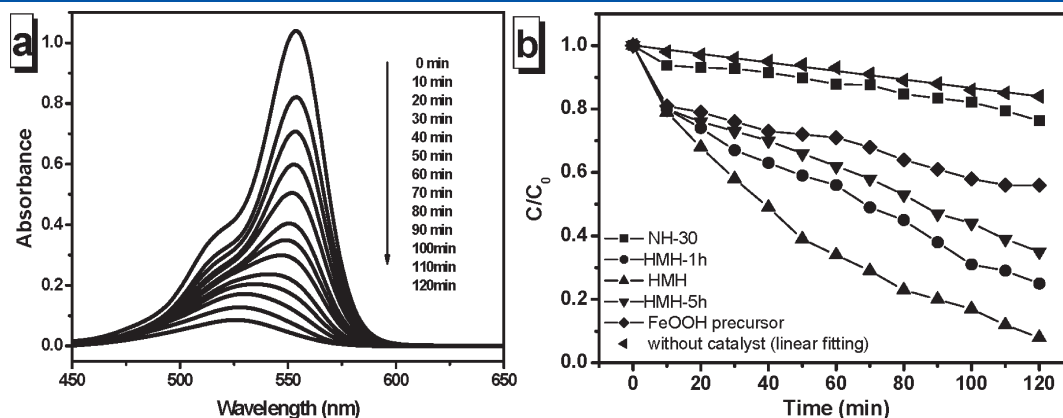


Figure 7. (a) Absorption spectra of a RB solution (1.0×10^{-5} M, 60 mL) in the presence of 30 mg hematite sample using high-pressure mercury lamp. (b) Photocatalytic performances with different additives at different time. HMH-1 h, HMH, HMH-5 h correspond to the FeOOH precursor annealing at 350 °C for 1, 3, and 5 h, respectively.

UV absorption spectrum in Figure 7a. It was shown that the absorbance of the RB solutions was decreased dramatically. Figure S4 of Supporting Information shows absorbance of Supporting Information of the RB solutions with other samples as catalysts. Compared with the results in Figure S4 of Supporting Information, the degradation rate of the HMH sample was up to 92% (calculated by the concentration ratio of RB solutions, related to the absorbance), higher than the degradation rate of other tested samples.

Figure 7b shows the degradation rates are 92, 75, 65, 44, 23, and 16% with different catalysts, corresponding to HMH, HMH-1 h, HMH-5 h, FeOOH precursor, NH-30, and without any catalyst, respectively. The HMH sample has nearly 6 times (92%/16%) as much degradation rate as that without any catalyst, bigger than other reported results.^{5,26} Undoubtedly, the as-prepared samples (including the FeOOH precursor and HMH series) are more efficient as photocatalytic agents than the purchased NH-30 sample because the fabricated hierarchical mesoporous samples with higher SSA (225 and 116 m²/g) than the NH-30 sample (47 m²/g) result in more unsaturated surface coordination sites exposed to the reactants. Especially, there are remarkable concentration decreases when using the HMH series and FeOOH precursor as catalysts in the first 10 min. It could attribute to more absorption amount of the RB molecules because of the higher surface area.

Why was the degradation rate using the HMH sample higher than using FeOOH precursor? On one hand, the formed “electron-transport channels” in the HMH sample by thermal annealing will reduce the recombination of photoinduced electron–hole pairs and be of great benefit to photocatalytic reaction. On the other hand, the hollow pore size of the HMH sample (7.85 nm) was bigger than that of the FeOOH precursor (3.85 nm), providing much more suitable space for the adsorption of RB molecules (its size is estimated to be 10 Å),³⁵ which caused increasing catalytic activities. Therefore, the degradation rate using HMH samples was higher than using FeOOH sample. Meanwhile, it is clear that HMH-1 h shows a reduced degradation ratio (75%) compared with the HMH sample (92%), as the electron-transport channels are not well built with shorter anneal time, although they have the similar morphology as revealed in Figure S5a of Supporting Information. As for the HMH-5 h with longer annealing time, the damaged hierarchical structure as shown in Figure S5b of Supporting Information might be the

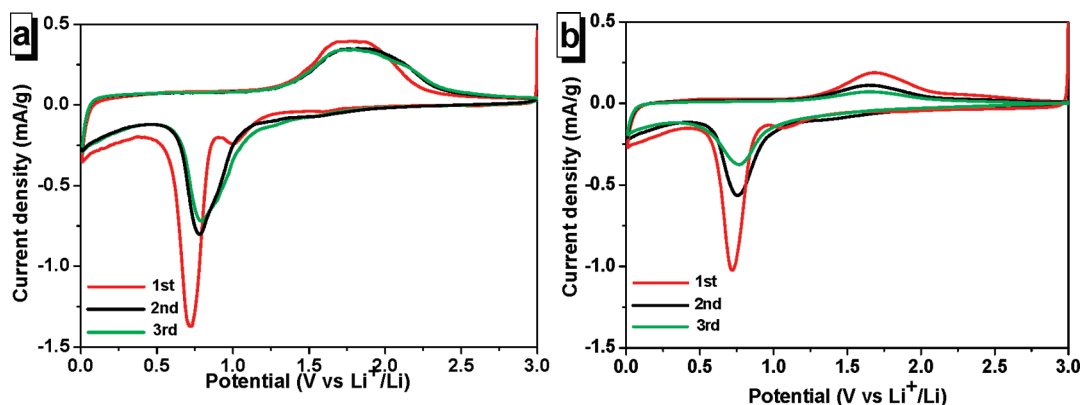
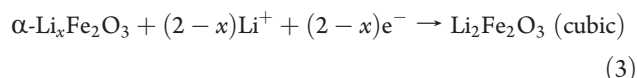
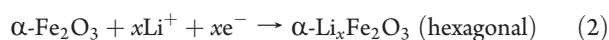


Figure 8. Cyclic voltammograms of the electrodes made from the HMH sample (a) and the NH-30 sample (b). The scan rate of the CV tests was 0.1 mV/s.

main reason for the reduced degradation rate. By contrast and analysis above, it is believed that the designed hierarchical mesoporous structure has a notable advantage in the field of photocatalysis.

It is reported that the morphology plays a positive role in the electrochemical properties of lithium ion batteries.^{36,37} Herein, the electrochemical behaviors of electrodes made from the HMH sample and the NH-30 sample were evaluated by CV and galvanostatic charge/discharge cycling. Figure 8 shows the CV curves of the HMH sample and the NH-30 sample. In the first negative scan for the HMH sample in Figure 8a, two small peaks at 1.6 and 1.0 V as well as an obvious peak at 0.72 V are observed, indicating the following three lithiation processes in sequence.^{38,39}



At first, a small amount of lithium can be inserted into the mesoporous nanoplates of the HMH sample without any change of the structure (eq 2). Then, further intercalation makes the hexagonal $\alpha\text{-Li}_x\text{Fe}_2\text{O}_3$ transform to cubic $\text{Li}_2\text{Fe}_2\text{O}_3$ (eq 3). The peak at 0.72 V corresponds to the complete reduction from Fe(II) to Fe(0) (eq 4) and the decomposition of the electrolyte. In comparison with the first cycle, the disappearance of the small peaks at 1.0 and 1.6 V in the second and third cycles can be attributable to an irreversible phase transformation from $\alpha\text{-Li}_x\text{Fe}_2\text{O}_3$ to $\text{Li}_2\text{Fe}_2\text{O}_3$.⁴⁰ The potential range from 1.68 to 1.86 V in the first positive scan shows the oxidation reactions from Fe(0) to Fe(III).

Compared with the result in Figure 8b, the CV curves in Figure 8a are more stable for the HMH electrode than those for the NH-30 sample after the second cycle, indicating enhanced stability during the lithiation and delithiation processes of the HMH sample. Higher current densities of the HMH sample can be observed in Figure 8a, revealing its higher capacity. The difference of the electrochemical properties between the HMH and the NH-30 samples can be explained in Figure 6. The impedance spectrum also displays lithium ion transfer behavior in half cells. The electrode made from the HMH sample has

better conductivity than that from NH-30 sample. Therefore, the HMH sample has an ideal structure for the transfer and storage of lithium ions.

The first three discharge–charge curves of the electrode made of the HMH sample at a low current rate of 0.05C (50 mA/g) were shown in Figure 9a. The discharge capacities are 1430, 1183, and 1144 mAh/g for the first, second, and third cycles, respectively. It is larger than the theoretical capacity of 1007 mAh/g, which can be the SEI (solid electrolyte interphase) layer forming by the decomposed electrolyte at low voltage and further lithium insertion via interfacial charging at metal/ Li_2O interfaces.^{41,42} As the HMH sample with high SSA and rich mesopores, the discharge capacities of the three cycles for the HMH electrode are still higher than the reported value of the electrode made of flowerlike hematite.⁵ The nearly overlap of the second and the third discharge curves shows that the morphology of the hematite electrode can keep stable during these cycles.

The cycling performances for the two samples with varied current rates were revealed in Figure 9b. They have the similar decreasing trends for the capacity along with the increasing current rates. However, the capacity difference between these two samples is reduced gradually. It can be ascribed to the structure collapse of the HMH sample at higher current rates, making an inconspicuous difference from the NH-30 sample. When the current rate rechanges to 0.05C, it is impressive to observe a specific storage capacity of 560 mAh/g after a 37-cycle discharge, much higher than 360 mAh/g of the NH-30 sample. It could be deduced that hierarchical mesoporous structure still exist partially in the HMH sample. A remarkable structure advantage of the HMH sample has been revealed in a long-time discharge process. Therefore, the as-obtained HMH sample is suitable for electrodes of lithium batteries with slow charge and discharge.

In conclusion, a hierarchical $\alpha\text{-FeOOH}$ precursor composed of porous nanoplates with a high SSA (up to 225 m^2/g) was fabricated by a mild wet chemical method using CTAB as the surface modification agent. The corresponding hematite sample has the similar morphology after thermal anneal, with a SSA of 116 m^2/g and an average pore size of 7.85 nm. The hematite particles in the nanoplates grew or linked together forming netlike substructures (like electron-transport channels) during heating. In consideration of the high surface area, rich mesopores, and channels of the hematite sample, photocatalytic performances with the degradation of RB and the electrochemical

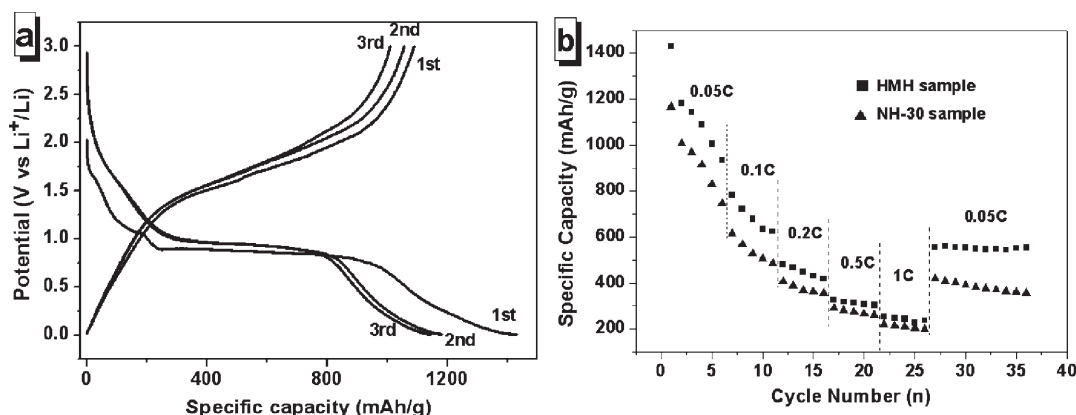


Figure 9. (a) The discharge–charge curves of the HMH electrode at a current rate of 0.05C (50 mA/g). (b) Rate capabilities of the HMH (squares) and NH-30 (triangles) samples at different current rates.

measurements in lithium ion batteries were carried out. The degradation rate of the as-prepared sample was up to 92%, while it is only 23% with hematite NPs, ~30 nm in diameter. Compared with the specific storage capacity of 360 mAh/g for the NPs, the hierarchical mesoporous sample has a much higher value of 560 mAh/g after 37 cycles. The remarkable improvement on the photocatalytic and electrochemical properties could attribute to the fabricated mesoporous three-dimension structure. It offers higher SSA with more unsaturated coordination sites for the adsorption and degradation of RB molecules, as well as netlike substructures for reduced recombination of photo-induced electron–hole pairs. It also improves the conductivity of the electrode, thus, it is in favor of transfer and storage of lithium ions. To sum up, the as-obtained hierarchical mesoporous structure does have a great benefit for the application in photocatalytic degradation and lithium ion batteries.

■ ASSOCIATED CONTENT

Supporting Information. TEM and HRTEM images of FeOOH precursor, SEM image and XRD pattern of the purchased NH-30 sample, SEM image of the hematite sample using less CTAB as soft templates, absorption spectra of RB solutions with the catalysts of NH-30, FeOOH precursor, HMH-1 h, and HMH-5 h, as well as SEM images of the HMH-1 h and HMH-5 h samples. This material is available free of charge via the Internet at <http://pubs.acs.org>.

■ AUTHOR INFORMATION

Corresponding Author

*E-mail: jhli@mail.tsinghua.edu.cn (J.L.); guolin@buaa.edu.cn (L.G.).

■ ACKNOWLEDGMENT

This work was financially supported by the National Basic Research Program of China (2011CB935704, 2010CB934700, and 2007CB310501), the National Natural Science Foundation of China (11079002, 50725208 and 20973019), the State Key Project of Fundamental Research for Nanoscience and Nanotechnology (2006CB932301), and the Research Fund for the Doctoral Program of Higher Education of China (No. 20101102120045).

■ REFERENCES

- (1) Zou, Z. G.; Ye, J. H.; Sayama, K.; Arakawa, H. *Nature* **2001**, 414, 625.
- (2) Asahi, R.; Morikawa, T.; Ohwaki, T.; Aoki, K.; Taga, Y. *Science* **2001**, 293, 269.
- (3) Wang, Z. L. *ACS Nano* **2008**, 2, 1987.
- (4) Yu, J.; Dai, G.; Cheng, B. *J. Phys. Chem. C* **2010**, 114, 19378.
- (5) Zeng, S. Y.; Tang, K. B.; Li, T. W.; Liang, Z. H.; Wang, D.; Wang, Y. K.; Qi, Y. X.; Zhou, W. W. *J. Phys. Chem. C* **2008**, 112, 4836.
- (6) Niu, M.; Huang, F.; Cui, L.; Huang, P.; Yu, Y.; Wang, Y. *ACS Nano* **2010**, 4, 681.
- (7) Wodka, D.; Bielańska, E.; Socha, R. P.; Elżbieciak-Wodka, M.; Gurgul, J.; Nowak, P.; Warszyński, P.; Kumakiri, I. *ACS Appl. Mater. Interfaces* **2010**, 2, 1945.
- (8) Formo, E.; Lee, E.; Campbell, D.; Xia, Y. *Nano Lett.* **2008**, 8, 668.
- (9) Yang, W.-H.; Lee, C.-F.; Tang, H. Y.; Shieh, D.-B.; Yeh, C.-S. *J. Phys. Chem. B* **2006**, 110, 14087.
- (10) Jia, C.-J.; Sun, L.-D.; Luo, F.; Han, X. D.; Heyderman, L. J.; Yan, Z.-G.; Yan, C.-H.; Zheng, K.; Zhang, Z.; Takano, M.; Hayashi, N.; Eltschka, M.; Kläui, M.; Rüdiger, U.; Kasama, T.; Cervera-Gontard, L.; Dunin-Borkowski, R. E.; Tzvetkov, G.; Raabe, J. *J. Am. Chem. Soc.* **2008**, 130, 16968.
- (11) Hu, X. L.; Yu, J. C.; Gong, J. M. *J. Phys. Chem. C* **2007**, 111, 11180.
- (12) Li, Z. M.; Lai, X. Y.; Wang, H.; Mao, D.; Xing, C. J.; Wang, D. *Nanotechnology* **2009**, 20, 245603.
- (13) Zhong, J. Y.; Cao, C. B. *Sens. Actuators, B* **2010**, 145, 651.
- (14) Sivula, K.; Zboril, R.; Formal, F. L.; Robert, R.; Weidenkaff, A.; Tucek, J.; Frydrych, J.; Grätzel, M. *J. Am. Chem. Soc.* **2010**, 132, 7436.
- (15) Sun, B.; Horvat, J.; Kim, H. S.; Kim, W.-S.; Ahn, J.; Wang, G. *J. Phys. Chem. C* **2010**, 114, 18753.
- (16) Wu, C.; Yin, P.; Zhu, X.; OuYang, C.; Xie, Y. *J. Phys. Chem. B* **2006**, 110, 17806.
- (17) Hermanek, M.; Zboril, R.; Medrik, I.; Pechousek, J.; Gregor, C. *J. Am. Chem. Soc.* **2007**, 129, 10929.
- (18) Zhong, L.-S.; Hu, J.-S.; Liang, H.-P.; Cao, A.-M.; Song, W.-G.; Wan, L.-J. *Adv. Mater.* **2006**, 18, 2426.
- (19) Cao, S.-W.; Zhu, Y.-J. *J. Phys. Chem. C* **2008**, 112, 6253.
- (20) Kim, H. S.; Piao, Y.; Kang, S. H.; Hyeon, T.; Sung, Y.-E. *Electrochem. Commun.* **2010**, 12, 382.
- (21) Hu, X. L.; Yu, J. C.; Gong, J. M.; Li, Q.; Li, G. *Adv. Mater.* **2007**, 19, 2324.
- (22) Hsu, L.-C.; Kuo, Y.-P.; Li, Y.-Y. *Appl. Phys. Lett.* **2009**, 94, 133108.
- (23) Das, M.; Mishra, D.; Dhak, P.; Gupta, S.; Maiti, T. K.; Basak, A.; Pramanik, P. *Small* **2009**, 5, 2883.
- (24) Ruan, H. D.; Frost, R. L.; Klopogge, J. T. *Spectrochim. Acta A* **2001**, 57, 2575.

- (25) Mandal, S.; Müller, A. H. E. *Mater. Chem. Phys.* **2008**, *111*, 438.
- (26) Zeng, S. Y.; Tang, K. B.; Li, T. W.; Liang, Z. H. *J. Phys. Chem. C* **2010**, *114*, 274.
- (27) Jiao, F.; Harrison, A.; Jumas, J.-C.; Chadwick, A. V.; Kockelmann, W.; Bruce, P. G. *J. Am. Chem. Soc.* **2006**, *128*, 5468.
- (28) Li, L.; Chu, Y.; Liu, Y.; Dong, L. *J. Phys. Chem. C* **2007**, *111*, 2123.
- (29) Kim, T. W.; Ha, H.-W.; Paek, M.-J.; Hyun, S.-H.; Baek, I.-H.; Choy, J.-H.; Hwang, S.-J. *J. Phys. Chem. C* **2008**, *112*, 14853.
- (30) Zhou, W.; Yao, M.; Guo, L.; Li, Y. M.; Li, J. H.; Yang, S. H. *J. Am. Chem. Soc.* **2009**, *131*, 2959.
- (31) Fink, J.; Kiely, C. J.; Bethell, D.; Schiffrin, D. J. *Chem. Mater.* **1998**, *10*, 922.
- (32) Shyue, J.-J.; De Guire, M. R. *J. Am. Chem. Soc.* **2005**, *127*, 12736.
- (33) Pradhan, M.; Sarkar, S.; Sinha, A. K.; Basu, M.; Pal, T. *J. Phys. Chem. C* **2010**, *114*, 16129.
- (34) Li, Y. M.; Li, J. H. *J. Phys. Chem. C* **2008**, *112*, 14216.
- (35) Qian, G. D.; Wang, M. Q. *J. Phys. D: Appl. Phys.* **1999**, *32*, 2462.
- (36) Reddy, M. V.; Yu, T.; Sow, C. H.; Shen, Z. X.; Lim, C. T.; Rao, G. V. S.; Chowdari, B. V. R. *Adv. Funct. Mater.* **2007**, *17*, 2792.
- (37) Jiao, F.; Bao, J. L.; Bruce, P. G. *Electrochem. Solid-State Lett.* **2007**, *10*, A264.
- (38) Larcher, D.; Masquelier, C.; Bonnin, D.; Chabre, Y.; Masson, V.; Leriche, J. B.; Tarascon, J. M. *J. Electrochem. Soc.* **2003**, *150*, A133.
- (39) Larcher, D.; Bonnin, D.; Cortes, R.; Rivals, I.; Personnaz, L.; Tarascon, J. M. *J. Electrochem. Soc.* **2003**, *150*, A1643.
- (40) Morales, J.; Sanchez, L.; Martin, F.; Berry, F.; Ren, X. L. *J. Electrochem. Soc.* **2005**, *152*, A1748.
- (41) Balaya, P.; Li, H.; Kienle, L.; Maier, J. *Adv. Funct. Mater.* **2003**, *13*, 621.
- (42) Jamnik, J.; Maier, J. *Phys. Chem. Chem. Phys.* **2003**, *5*, 5215.